Boosting the Performance of WO_3/n-Si Heterostructures for Photo-electrochemical Water Splitting: from the Role of Si to Interface Engineering

*Yihui Zhao, Geert Brocks, Han Genuit, Reinoud Lavrijsen, Marcel A. Verheijen, Anja Bieberle-Hütter**

Y. Zhao, H. Genuit, Dr. A. Bieberle-Hütter
Electrochemical Materials and Interfaces (EMI),
Dutch Institute for Fundamental Energy Research (DIFFER),
5600 HH Eindhoven, The Netherlands
E-mail: A.Bieberle@differ.nl

Prof. Dr. G. Brocks
Center for Computational Energy Research,
Department of Applied Physics, Eindhoven University of Technology,
P.O. Box 513, 5600MB Eindhoven, The Netherlands

Prof. Dr. G. Brocks
Computational Materials Science,
Faculty of Science and Technology and MESA+ Institute for Nanotechnology,
University of Twente,
P.O. Box 217, 7500 AE Enschede, The Netherlands

Dr. R. Lavrijsen
Physics of Nanostructures (FNA),
Department of Applied Physics,
Eindhoven University of Technology,
5600 MB Eindhoven, The Netherlands

Dr. M.A. Verheijen
Plasma and Materials Processing (PMP),
Department of Applied Physics, Eindhoven University of Technology,
5600 MB Eindhoven, The Netherlands

Keywords: Si, WO_3/n-Si, PEC water splitting, photovoltage

Abstract: Metal oxide/Si heterostructures make up an exciting design route to high performance electrodes for photo-electrochemical (PEC) water splitting. By monochromatic light sources, contributions of the individual layers in WO_3/n-Si heterostructures are untangled. It shows that band bending near the WO_3/n-Si interface is instrumental in charge separation and transport, and in generating a photovoltage that drives the PEC process. A thin metal layer inserted at the WO_3/n-Si interface helps establishing the relation among the band bending depth, the photovoltage, and the PEC activity. This discovery breaks with the dominant Z-scheme

design idea, which focusses on increasing the conductivity of an interface layer to facilitate charge transport, but ignores the potential profile around the interface. Based on the analysis, a high work function metal is predicted to provide the best interface layer in WO_3/n-Si heterojunctions. Indeed, the fabricated WO_3/Pt/n-Si photoelectrodes exhibit a 2 times higher photocurrent density at 1.23 V vs RHE and a 10 times enhancement at 1.6 V vs RHE compared to WO_3/n-Si. Here, it is essential that the native SiO_2 layer at the interface between Si and the metal is kept in order to prevent Fermi level pinning in the Schottky contact between the Si and the metal.

1. Introduction

Hydrogen production from photoelectrochemical (PEC) water splitting provides a promising pathway for converting solar energy to chemical fuels[1–4]. A key element of any PEC system is the semiconductor material, which transforms absorbed solar photons into excited electronic states[5]. Among all the semiconductor materials, metal oxides, such as TiO_2, WO_3, Fe_2O_3, and $BiVO_4$, have been studied elaborately as the functional layer for catalyzing PEC water splitting reactions because of their chemical stability and low cost[6–14]. To supply sufficient energy (including overpotential) for splitting water, the band gaps of metal oxides tend to be substantial (≥ 1.9) [3], which limits their absorption of solar light, however.

Silicon (Si) is a widely available commercial semiconductor; it is easily structured, has a controllable electrical conductivity, and is suitable as substrate for functional films[15]. In addition, Si has a moderate band gap (1.1 eV), and a light absorption that matches the solar spectrum reasonably well[16]. On the down side, Si has a poor chemical stability, because it is rapidly oxidized in aqueous solution under solar illumination or under anodic bias[17]. Covering a Si substrate with a metal oxide film improves the chemical stability and offers a promising model for PEC electrode design. Indeed, recent research has produced several studies on metal oxide/Si heterojunction photoelectrodes for PEC water splitting, such as TiO_2/Si[18], Fe_2O_3/Si[19]

and WO_3/Si[20,21]. These studies have concentrated on the absorption of the visible part of the sunlight by Si, and the contribution to the PEC process of the subsequent photogenerated charges in Si.

To further improve the PEC performance of such photoelectrodes, light harvesting and surface reactions can be enhanced through nano- or micro-structuring, in the form of nanowire (NW) or micro-pillar structures, coated with metal oxide films [6,15,22–28]. TiO_2/NWs Si showed a 2.5 times higher photocurrent density than planar TiO_2/Si[6]. Fe_2O_3/NWs Si exhibited a current density of about 0.9 mA/cm^2 at 1.23 V vs RHE, which was 2.5 times higher than that of planar Fe_2O_3/FTO (FTO, fluorine doped tin oxide)[23]. Moreover, to improve water oxidation kinetics, co-catalysts such as CoO_x, Co-Pi or Ir, were introduced on the surface of metal oxide/Si photoelectrodes[18,29,30].

Besides considering such micro/nano-structures or co-catalysts, it is important to understand the more fundamental issue by how much the Si contributes to the PEC process. Whereas the holes photogenerated in the metal oxide layer are used in the water oxidation reaction at the anode, their electron partners have to move from the metal oxide layer to the Si and from there to the counter electrode for the water reduction reaction. For TiO_2/n-Si, Fe_2O_3/n-Si, and WO_3/n-Si, a Z scheme mechanism was invoked to describe the charge transfer at the metal oxide-Si interface, where the electrons from the oxide layer recombine with holes photogenerated in Si. Note that this mechanism should also reduce the electron-hole recombination within the metal-oxide layer[6,21,23,31].

The Z scheme provides a general framework, but the exact roles of the metal-oxide layer and the Si substrate in its functioning have not investigated so far. In order to further improve the efficiency of the metal oxide/Si photoelectrodes, it is important to understand the contributions of the individual layers in the heterojunction to the PEC water splitting. To this aim, we evaluate in this study the decoupled contributions of the metal-oxide layer and Si

substrate experimentally. In particular, we elucidate how the Si contributes to the overall process. We select WO_3 as the metal-oxide layer because of its high electron mobility (~12 $cm^2V^{-1}s^{-1}$ at RT) and because its band-gap (2.6-2.9 eV)[12,32] is significantly higher than that of Si (~ 1.1 eV)[29]. This difference in band gaps allows us to use IR light to selectively excite Si, whereas UV light can be used to excite WO_3. In particular, to study the relation between the heterojunction band structure and the PEC activity, chopped monochromatic light illumination is used to measure the change of the open circuit voltage (V_{OC}), which reflects the generated photovoltage during PEC water splitting.

Within the Z scheme one can insert a thin metal layer at the heterojunction, which is believed to promote the electron transfer between the two semiconductors. We study the impact of such metal layers in WO_3/n-Si heterojunction photoelectrodes on the PEC water splitting, using a metal with a moderate work function (Ag) and one with a high work function (Pt) as examples. In particular, we study the role of the native SiO_2 layer on preventing unwanted Fermi level pinning at the metal-Si Schottky contact. We gain a systematic insight into the role of Si in WO_3/Si heterojunctions, which guides towards design rules for high performance photoelectrodes.

2. Results and Discussion

2.1. WO_3/n-Si heterojunctions

SEM images of the surface morphologies and the cross-sections of WO_3/n-Si and WO_3/FTO after annealing in Ar, are shown in **Figure 1**. The surface of WO_3/n-Si is homogeneous with some micro-cracks (Figure 1a). In contrast, the surface morphology of WO_3/FTO shows a grainy structure with holes between the grains (Figure 1b). This is because the WO_3 film is coated on the FTO grains and thus reproduces the morphology of the FTO. The surface roughnesses of WO_3/n-Si and WO_3/FTO are R_a = 2.2 nm and R_a = 7.1 nm, respectively,

which were measured by Atomic Force Microscope (AFM) (Figure S2). Hence, the WO_3/FTO photoelectrodes have a higher specific surface area, which has been proven to be beneficial to the PEC activity[32,33]. From the cross section images (Figure 1c and 1d), it can be seen that the WO_3 films are well adhered to the substrates for both WO_3/n-Si and WO_3/FTO. The thicknesses of the WO_3 layers are around 200 nm. High-resolution TEM images (Figure 1e and 1f) show that both WO_3/n-Si and WO_3/FTO have an intimate contact between the WO_3 film and the substrate (HAADF-STEM in Figure S3). Typically, a ~4 nm native SiO_2 layer is detected at the interface of WO_3/n-Si. According to Figure S4, the diffraction peaks of the films on all substrates agree well with monoclinic WO_3 (JCPDS No. 83-0950), indicating that monoclinic WO_3 is obtained for both electrodes after annealing.

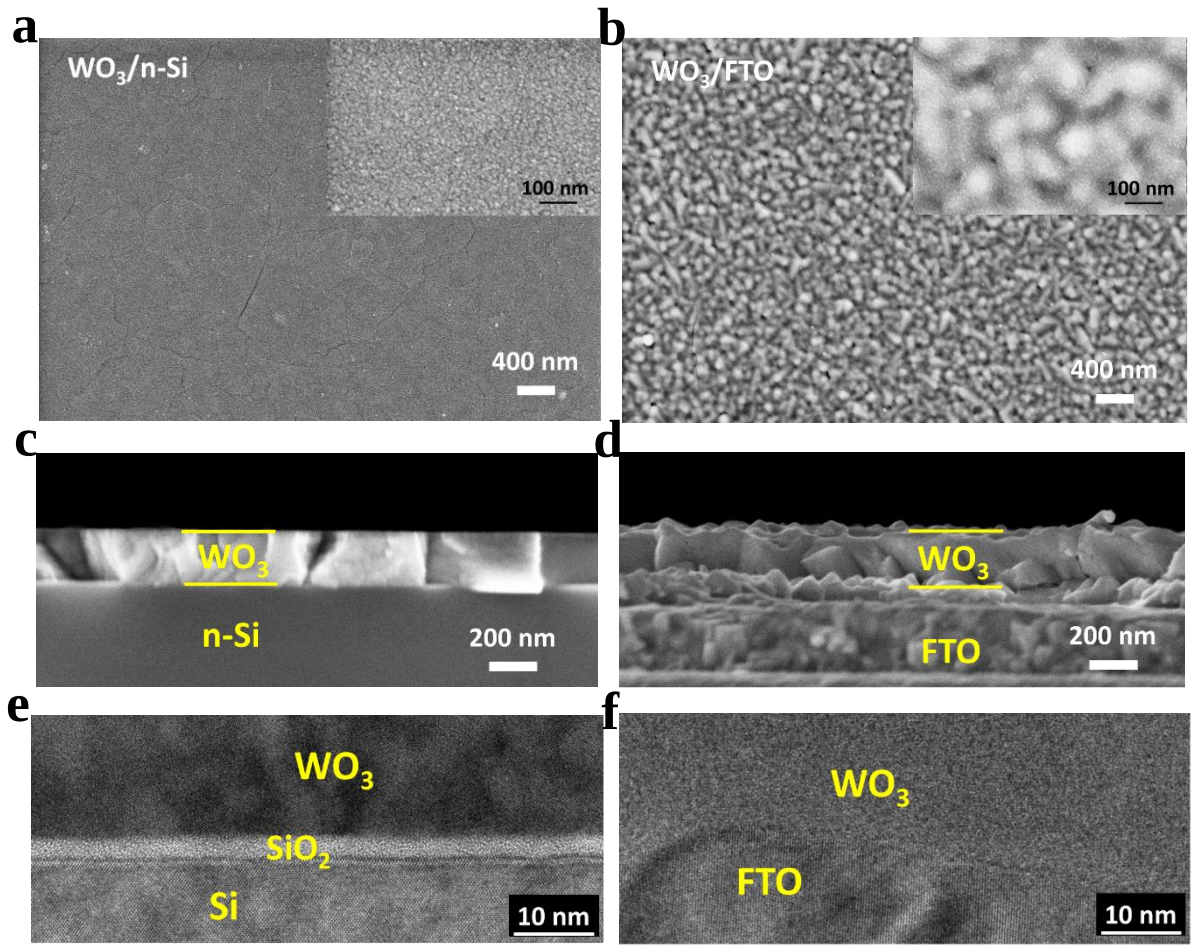

Figure 1. Scanning Electron Microscopy images of surface morphology (a) (b) and cross-sections (c) (d) of WO_3/n-Si (a) (c) and of WO_3/FTO (b) (d); Interface cross-sectional high-resolution TEM images of (e) WO_3/n-Si and (f) WO_3/FTO.

The photocurrents as a function of the applied potential (0.4 - 1.6 V vs RHE) were measured in 0.5 M H_2SO_4 under chopped AM 1.5 illumination. As shown in **Figure 2**, the WO_3/n-Si photoelectrode has a photocurrent density of 0.12 mA/cm^2 at 1.23 V vs RHE. This is about double the photocurrent density of 0.06 mA/cm^2 at 1.23 V vs RHE obtained for the WO_3/FTO electrode, even though the latter has a larger specific surface area (Figure S2). Moreover, the WO_3/n-Si electrode exhibits a photocurrent onset potential as low as 0.4 V vs RHE, which is significantly lower than the 0.75 V vs RHE found for the WO_3/FTO electrode. In the literature, photocurrent densities between 0.03 mA/cm^2 and 0.1 mA/cm^2 at 1.23 V vs RHE have been observed for sputtered WO_3/FTO electrodes, with onset potentials of 0.7-0.75 V vs RHE[34,35].

A more detailed look at the voltammogram under chopped light at 0.4 - 0.7 V vs RHE is given in the inset in Figure 2. With the WO_3/n-Si electrode, the photocurrent increases rapidly when the light is switched on, and then shows a transient decay. If the applied potential is large, there is no significant transient decay. A decay of photocurrents suggests a recombination of the photogenerated carriers and indicates that not all photogenerated carriers are transported completely to the back contact at low applied potential. Such transient currents are not observed with the WO_3/FTO electrode. We conclude that there are more electrons and holes generated with the WO_3/n-Si electrode. The n-Si in WO_3/n-Si electrodes absorbs light that penetrates through the WO_3 film and contributes photogenerated carriers to the circuit during PEC water splitting.

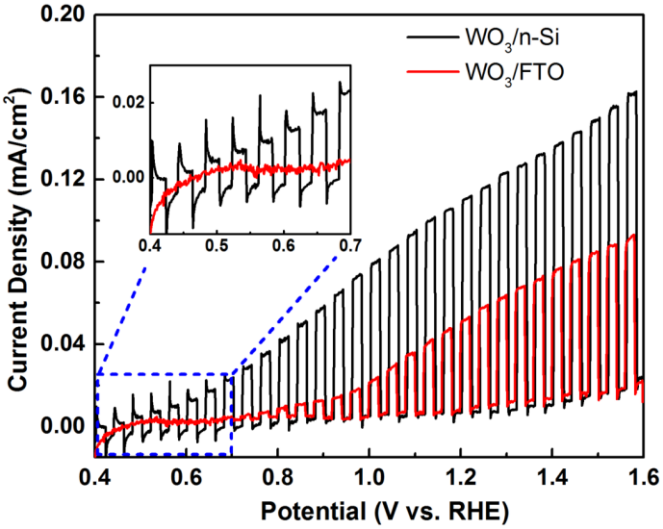

Figure 2. Photocurrent density vs. applied potential curves under chopped simulated sun light illumination (light intensity: 100 mW cm^{-2}; cycles of 2s light on and 2s light off; electrolyte: 0.5 M H_2SO_4) for WO_3/n-Si (black) and WO_3/FTO (red). (Inset: enlargement of the curves at 0.4 – 0.7 V vs. RHE).

2.2. PEC measurements under monochromatic light

In order to decouple the contribution of the n-Si from WO_3, we carried out PEC measurements with monochromatic light illumination. The idea is that due to the different bandgaps of n-Si (~ 1.1 eV[29]) and WO_3 (~3.0 eV from our previous work[36]) one or the other materials can be excited selectively by a light source. A UV lamp with λ = 365 nm and an IR laser with λ = 980 nm were chosen to excite the WO_3 and the n-Si, respectively. **Figure 3**a shows a schematic sketch of the set-up. A long-pass dichroic mirror (cut-off wavelength 600 nm) was used to make sure that the UV and the IR beams can be combined to illuminate the same spot on the electrode.

Figure 3b shows the photocurrent densities as a function of the applied potential for three different illuminations: UV, IR, and UV+IR. The photocurrent density under UV illumination (pink curve) is 9.2 $\mu A/cm^2$ at 1.23 V vs. RHE. The photocurrent density under IR illumination (red curve) is close to the dark current indicating that photogenerated charge carriers in Si are not used directly in the water splitting process. When a combined UV and IR beam illuminates the electrode (blue curve), the photocurrent density is 18.1 $\mu A/cm^2$ at 1.23 V

vs. RHE. This is about two times higher than the photocurrent density under UV illumination alone. From these three different illuminations, we conclude that photogenerated charge carriers in Si contribute to the water oxidation, but indirectly, meaning that the holes generated in Si are not transferred to participate in the electrochemical reactions at the WO_3/electrolyte interface.

The charge transport in WO_3/n-Si during the PEC process is best discussed using the energy band diagrams shown in Figure 3c and d. Both Si and WO_3 are n-type semiconductors, where the work function of WO_3 is approximately 1 eV higher than that of Si (Figure S5). Therefore, to achieve equilibrium (in the dark) between the chemical potentials of Si and WO_3, the bands bend upwards going across the Si/WO_3 interface (Figure 3c). The H_2O/O_2 oxidation potential lies below the chemical potential of WO_3 (Figure S5), which means that to obtain equilibrium, the WO_3 bands bend upwards at the WO_3/electrolyte interface going from the metal oxide to the electrolyte (Figure 3c).

Under combined UV+IR illumination (Figure 3d), electrons and holes are generated both in Si and in WO_3. The photogenerated holes in WO_3 move towards the WO_3/electrolyte interface, while the electrons move towards the WO_3/n-Si interface, each of them following the built-in field as represented by the band bending in Figure 3c. Meanwhile, the photogenerated holes in n-Si move towards the WO_3/n-Si interface and partially recombine with the electrons from the WO_3. To complete the circuit, the photogenerated electrons in n-Si move to the counter electrode for the water reduction reaction. The overall charge transport process just described is called a Z scheme and has already been discussed for TiO_2/n-Si[6] and Fe_2O_3/n-Si[23] photoelectrodes. The Z scheme reduces the recombination of the photogenerated electrons and holes inside the metal oxide layer, which was considered to be the crucial reason for the enhancement of the PEC activity. However, the Z scheme also promotes a charge separation between holes in the metal oxide and electrons in the Si. Hence, it also creates a photovoltage across the metal oxide/Si junction. This contributes to the driving force and increases the

photocurrent. The influence of this photovoltage on the PEC activity has not been identified so far.

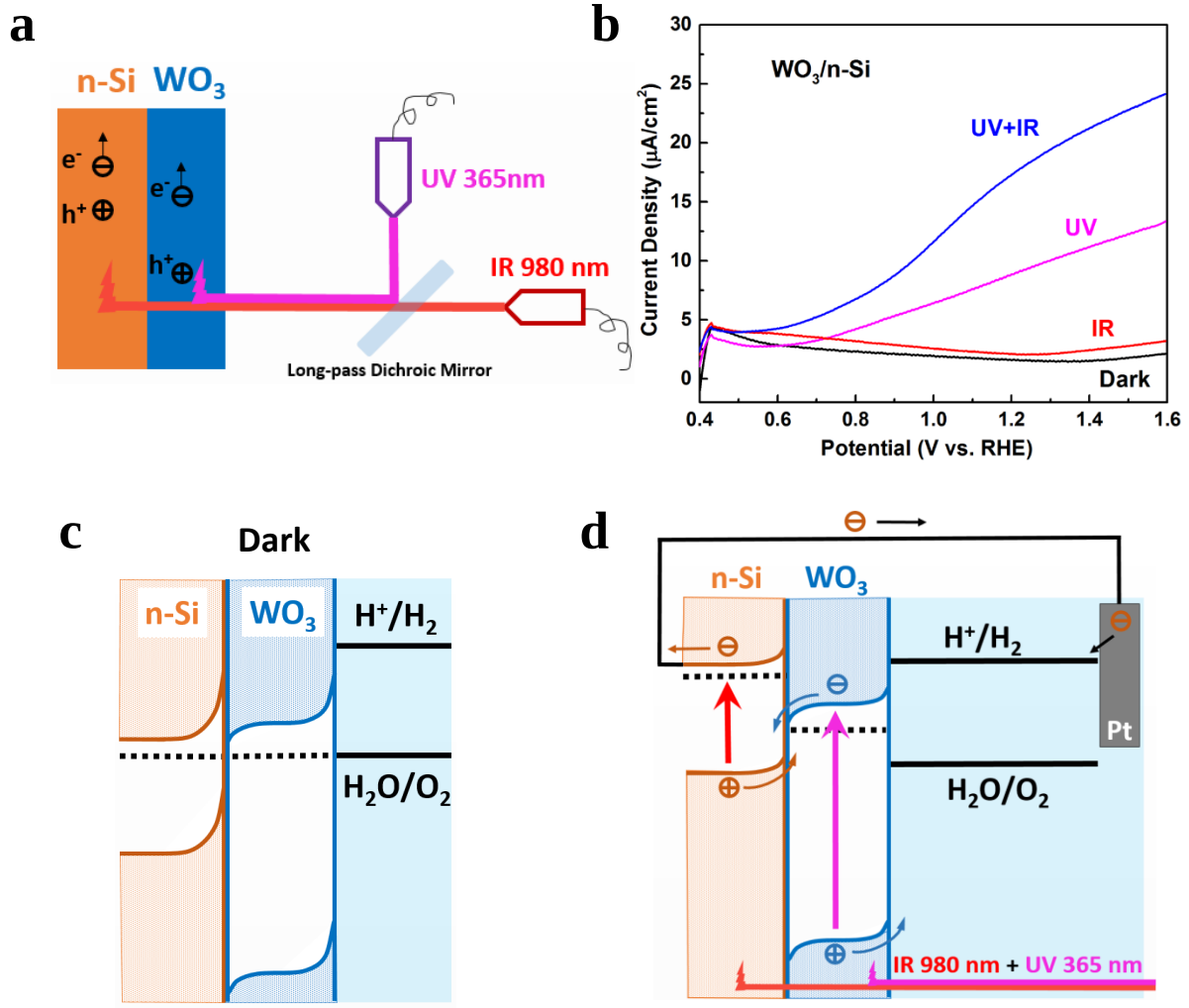

Figure 3. (a) Schematic drawing of the set-up for monochromatic light illumination of WO_3/n-Si. (b) Photocurrent density vs. applied potential under monochromatic light illumination of WO_3/n-Si. (c) Schematic energy band diagram in the dark under equilibrium. (d) Energy band diagram under illumination.

2.3. Photovoltage under chopped monochromatic light

The photovoltage created in the circuit can be determined by the change of the open circuit potential (V_{OC}) under illumination. We measure the V_{OC} of the WO_3/n-Si heterostructure under separate monochromatic chopped UV and IR illumination (**Figure 4**a). Under chopped UV illumination, the V_{OC} shows a cathodic shift of 0.05 V, from 0.54 to 0.49 V vs RHE (purple curve in Figure 4a), when the UV light is switched on. Under chopped IR illumination, the V_{OC}

shows a cathodic shift of 0.11 V, from 0.54 to 0.43 V vs RHE (red curve in Figure 4a), when the IR is switched on. The V_{OC} shift under chopped IR illumination is double as large as that under chopped UV illumination. If the chopped UV is combined with a continuous IR illumination, the V_{OC} shows an additional cathodic shift of ~0.007 V only (blue curve in Figure 4a), when the UV is switched on. This is significantly smaller than that under chopped UV illumination only (purple curve).

The change of the V_{OC} under chopped illumination is illustrated by the band diagrams in Figures 4b and c. When the UV is switched on (Figure 4b), electron-hole pairs are generated in the WO_3 layer. The built-in field resulting from the space charges drives the holes towards the electrolyte, and the electrons towards the WO_3/n-Si interface. The electrons are then partly injected into the Si and recombine with available holes there. The charge separation just described shifts the Fermi levels E_F (dashed thick lines in Figure 4b) of the WO_3 and n-Si upward. Therefore, when the UV light is switched on, the V_{OC} of the WO_3/n-Si photoanode shows a cathodic shift (Figure 4a). Under IR illumination (Figure 4c), electron-hole pairs are generated in Si only. The holes migrate in the build-in field towards the interface with WO_3 and partly recombine with available electrons in WO_3. Therefore, the Fermi level E_F in n-Si shifts upward and that in WO_3 shifts downward, which results in a more cathodic V_{OC}.

If a chopped UV light is added on a continuous IR illumination, the two processes for charge generation and separation as discussed in the previous paragraph (Figures 4b and 4c) are both active. The Fermi level in Si is, however, predominantly determined by the continuous IR illumination. When UV light is switched on additionally, more electrons, photogenerated in WO_3, inject into Si, but this does not increase the Fermi level in Si much further. Therefore, the V_{OC} shift is then comparable to that under IR illumination only, and much larger than under UV illumination only.

The results above indicate that, under illumination, the Fermi level shift in n-Si makes an important contribution to the photovoltage created in the WO_3/n-Si system. The photovoltage can be added to the circuit voltage. It thus enhances the thermodynamic driving force on the charge transport in a PEC cell[37] and increases the overall photocurrent.

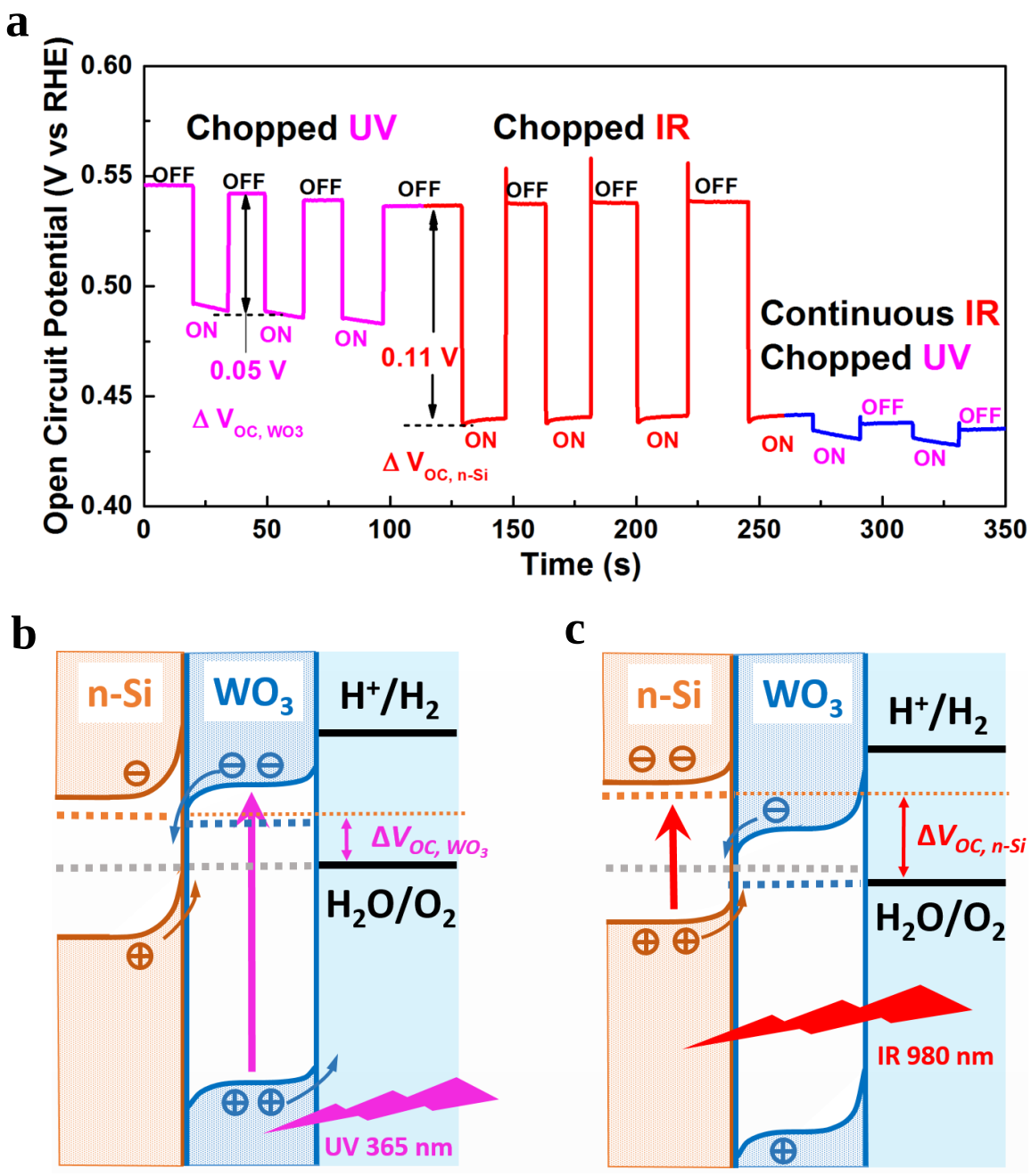

Figure 4. (a) Open circuit potential (V_{OC}) versus elapsed time for WO_3/n-Si under chopped UV illumination (purple), chopped IR illumination (red), and chopped UV with a continuous IR illumination (blue). Schematic energy band diagrams and ΔV_{OC} of WO_3/n-Si under UV (b) and under IR (c) illumination.

2.4. Ag interface layer

A thin metal layer is inserted between the two semiconductor layers within the Z scheme with the aim to function as an electron transport layer. It is reported that Ag acts as a Z scheme bridge in charge carrier migration to enhance the photocatalytic efficiency in the photocatalyst systems $Ag_3PO_4/Ag/WO_{3-x}$[38], AgBr/Ag/TiO_2[39] and AgBr/Ag/BiOBr[40]. However, a metal layer does not only affect charge carrier migration through enhancing the conductivity, but also sets up Schottky barriers with the surrounding semiconductors and impacts the band bending in those semiconductors. Such alterations in the potential profile may have substantial effects on charge separation, on the photovoltage, and, hence, on the PEC activity.

To test this, we have inserted an ultra-thin Ag layer (~5 nm) between the WO_3 layer and the n-Si. The relative energy bands and Fermi levels of n-Si, Ag, and WO_3 are shown in Figure S5. The work function of Ag is 4.5 ± 0.12 eV vs vacuum level[41], which is between the work functions of n-Si (4.25 ± 0.1 eV) and of WO_3 (5.25 ± 0.1 eV). As reported, for the interface of Ag/n-Si, the Ag can penetrate to the Si and can form a low contact resistivity[42]. Since the work function of the Ag layer is originally located between the n-Si and the WO_3, the band structure in equilibrium will not be influenced, no matter whether the Ag can diffuse to the Si or not. Hence, it is possible in principle that the Ag layer works as an electron mediator to enhance the Z scheme charge transport process. The Ag layer also sets up a Schottky barrier contact with respect to the n-Si. The difference in work functions of the two materials before contact determines the size of the band bending in n-Si after contact. Therefore, the band bending in n-Si in the WO_3/Ag/n-Si system should be substantially smaller than in the WO_3/n-Si system, see **Figure 5**a. It should be noted that the native SiO_2 layer was not removed before deposition of Ag onto n-Si in order to prevent Fermi level pinning. We will come back to this point later.

As the potential profile induced by band bending is instrumental in charge separation and in setting up a photovoltage, this strongly suggests that the photovoltage created in WO_3/Ag/n-Si should be smaller than that in WO_3/n-Si. This is confirmed by the result of the V_{OC} measurement of WO_3/Ag/n-Si under chopped monochromatic IR illumination, as shown in Figure 5b. When the IR is switched on, the V_{OC} shifts negatively with 0.06 V, which is about half the value found for WO_3/n-Si (ΔV_{OC} = 0.11 V, red part in Figure 4a).

The Ag layer in WO_3/Ag/n-Si then potentially has two opposing effects on the PEC water splitting. A decrease of the photovoltage should decrease the PEC activity, whereas the enhancement of the Z scheme charge migration should increase it. To identify which factor plays the dominant role, Figure 5c shows a comparison of the photocurrent density vs potential for WO_3/Ag/n-Si and WO_3/n-Si under chopped simulated sunlight illumination. For WO_3/Ag/n-Si, the photocurrent density is 0.05 mA/cm^2 at 1.23 V vs RHE, which is significantly lower than that of WO_3/n-Si. This result indicates that, instead of the Z scheme argument, the dominant role is played by the induced photovoltage, determined by the band bending in n-Si.

In addition, a detailed look at the curves at lower applied potential indicates that higher transient spikes are seen for WO_3/Ag/n-Si compared with WO_3/n-Si, which implies a higher recombination rate of photogenerated carriers. It supports the conclusion that the higher photovoltage created in WO_3/n-Si provides a stronger driving force for the separation of photogenerated charge carriers and thus enhances the PEC water splitting performance.

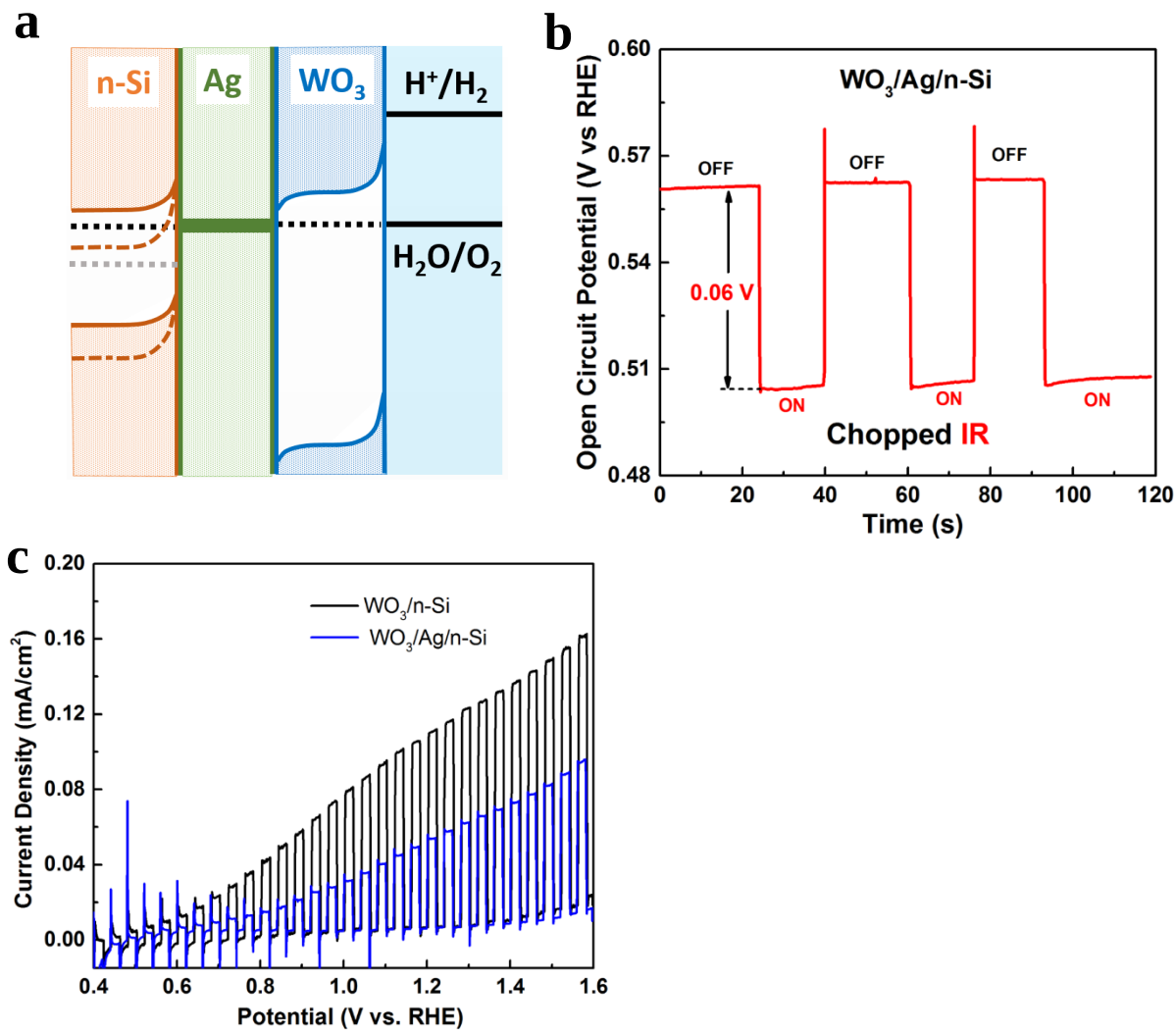

Figure 5. (a) Schematic band diagram of WO_3/Ag/n-Si in equilibrium in the dark; the dotted band lines indicate the band bending of Si in WO_3/n-Si, i.e., without the Ag interface layer. (b) Open circuit potential (V_{OC}) versus elapsed time for WO_3/Ag/n-Si under chopped IR illumination. (c) Photocurrent density vs. applied potential curves under chopped simulated sun light illumination (cycles of 2s light on and 2s light off) for WO_3/Ag/n-Si (blue) compared with WO_3/n-Si (black).

2.4. Interface states

When studying metal oxide/n-Si interfaces, one needs to consider that an ultrathin, native SiO_2 layer on Si is always present. It is known that this SiO_2 layer on Si may work as a passivation layer. SiO_2 layers can passivate surface states caused by the dangling bonds of Si, which cause Fermi level pinning in the Schottky barrier formation with metal contacts[43]. Here, we design experiments to study the effect of the native SiO_2 in WO_3/metal/n-Si electrode for PEC water splitting. We compare interfaces with and without native SiO_2 layer.

An ion beam milling (IBM) system was used to prepare substrates without SiO_2 layer (Figure S1). As the IBM system is directly connected to the sputter chamber, we do not have to break the vacuum and the metal layer can be deposited so that no oxide layer develops. In-situ X-ray photoelectron spectroscopy (XPS) was used to check the valence state of the Si after IBM treatment. **Figure 6**a shows the Si2p spectrum of the original n-Si. The peak of 99.5 eV is assigned to elemental Si and the peak of 103.1 is assigned to SiO_2[44,45]. Only a single elemental Si peak at 99.5 eV was detected for IBM treated n-Si (Figure 6b) which confirms that the SiO_2 layer was removed by the IBM treatment. The WO_3/Ag/n-Si photoelectrode without SiO_2 layer, is called WO_3/Ag/(IBM)n-Si in the following.

Figure 6c shows the band structure of Ag/(IBM)n-Si equilibrium in dark. When the Ag gets in contact with the clean Si surface, the Fermi level is pinned by midgap interface states. The resulting band bending in n-Si is actually comparable to that in the Ag/SiO_2/n-Si contact discussed above. This is confirmed by the result of the V_{OC} measurement of WO_3/Ag/(IBM)n-Si under chopped monochromatic IR illumination (Figure 6d). When the IR is switched on, the V_{OC} shifts negatively by 0.05 V, which is comparable to that of WO_3/Ag/n-Si (0.06 V, Figure 5b). However, comparing Figure 6d (WO_3/Ag/(IBM)n-Si) with Figure 5b (WO_3/Ag/n-Si), the IR light-on part of the curve shows more distinct transient spikes for WO_3/Ag/(IBM)n-Si (Figure 6d), which reveals a higher recombination of photogenerated electrons and holes; we attribute these to the presence of midgap states at the Ag/n-Si interface[46,47]. Figure 6e shows the comparison of the photocurrent density vs potential for WO_3/Ag/(IBM)n-Si and WO_3/Ag/n-Si under chopped simulated sunlight illumination. The photocurrent density in WO_3/Ag/n-Si is significantly higher than that in WO_3/Ag/(IBM)n-Si. We suggest that the native SiO_2 works as a passivation layer, which reduces the recombination rate of photogenerated electrons and holes at the interface of Ag and n-Si in WO_3/Ag/n-Si. We conclude therefore that, the native oxide SiO_2 should be retained for the fabrication of metal oxide/metal/Si photoelectrodes.

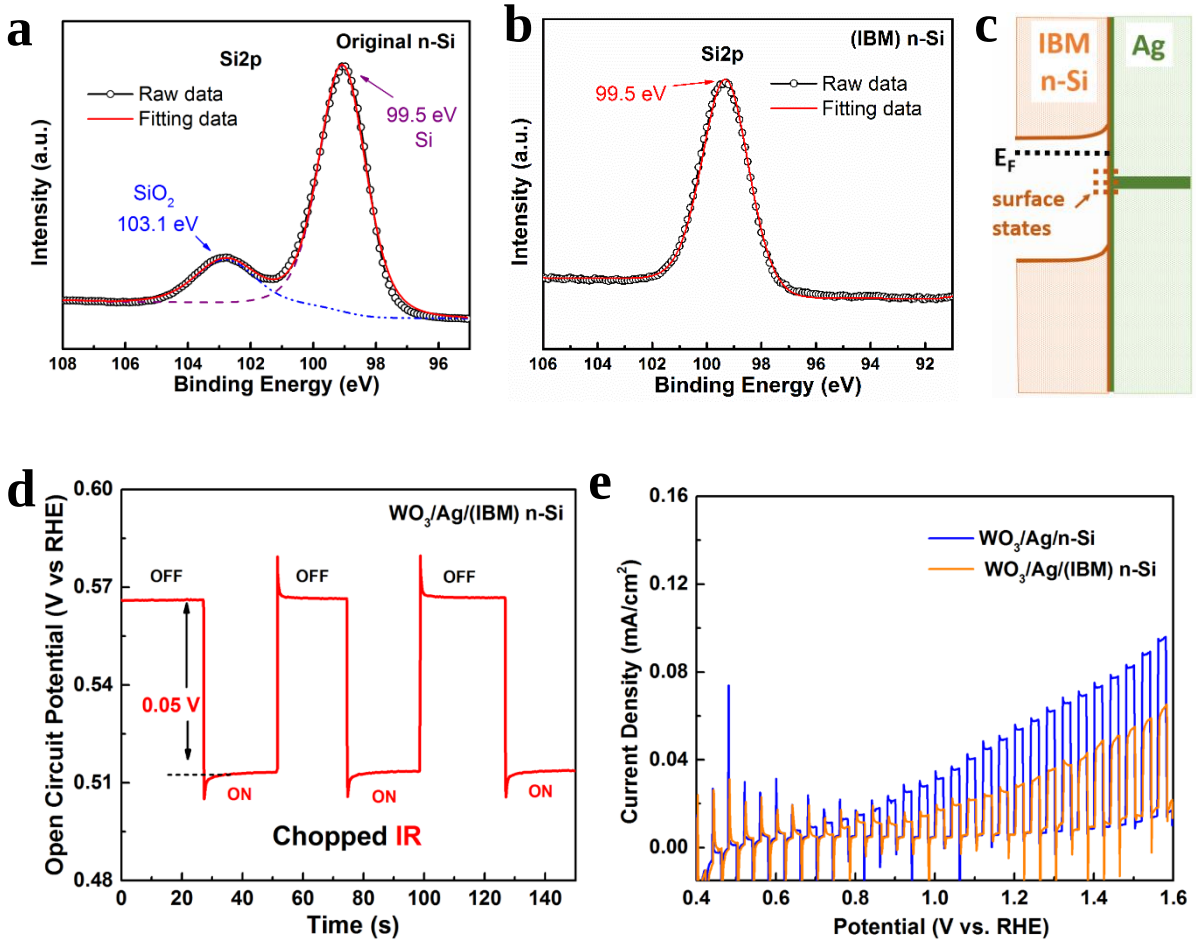

Figure 6. (a) (b) Si2p XPS spectra of n-Si: (a) original; (b) after ion beam milling (IBM). (c) Schematic Ag/(IBM)n-Si band diagram in equilibrium in the dark. (d) Open circuit potential (V_{OC}) versus elapsed time for WO_3/Ag/(IBM)n-Si under chopped IR illumination. (e) Photocurrent density vs. applied potential curves under chopped simulated sun light illumination (cycles of 2s light on and 2S light off) for WO_3/Ag/(IBM)n-Si (orange) compared with WO_3/Ag/n-Si (blue).

2.4. Pt interface layer

Based on the results discussed above, the native SiO_2 layer on the n-Si needs to be kept as a passivation layer. However, the Ag layer should be replaced by another metal with a higher work function to increase the extent of the n-Si band bending and thus enhance the PEC performance of WO_3/n-Si. Following this rule, we select Pt as the metal layer between the WO_3 and Si. **Figure 7**a shows the cross-section HAADF-STEM image of WO_3/Pt/n-Si. Pt is well adhered to the WO_3 and to the native SiO_2 layer. Holes can be detected in the Pt layer due to the thin thickness. Typically, there is a gradient diffusion layer of Pt detected in the Si below

the SiO_2 layer. This is because the Pt diffuses through the pinholes in SiO_2 layer to react with Si and forms a Pt doped Si (Pt-Si) layer during the annealing process[48]. The diffusion of Pt resulted in a small shift of the Fermi level of n-Si towards the valence band[49]. Figure 7b shows a diagram of relative energy band levels of n-Si, Pt-Si, Pt and WO_3. The work function of Pt is 5.7 ± 0.1 eV vs vacuum level[41], which means that the Fermi level of Pt lies below that of WO_3 (5.25 ± 0.1 eV). The Fermi level of Pt-Si is located between the Fermi level of n-Si and the work function of Pt. Figure 7c shows the energy band diagram in dark of WO_3/Pt/n-Si in equilibrium. The Pt-Si layer forms two Schottky contacts with the n-Si bulk and the Pt layer, which benefits the charge transport between the Si and Pt. The large difference between the Pt work function and the n-Si bulk Fermi level (4.25 ± 0.1 eV) before contact results in a higher photovoltage under illumination compared to the WO_3/n-Si, which can act as the driving force for charge transport.

The increase of the photovoltage is confirmed by the V_{OC} measurement of WO_3/Pt/n-Si under chopped monochromatic light illumination as shown in Figure 7d. Under chopped IR illumination (red curve in Figure 7d), the V_{OC} shifts by 0.32 V, which is about three times higher than in WO_3/n-Si (0.11 V, red curve in Figure 4a). Arc-shaped V_{OC} curves (purple curve in Figure 7d) are observed in WO_3/Pt/n-Si under chopped UV illumination, which implies a delay in the charge transport. This can be due to a Schottky barrier Φ_B that is generated at the interface of WO_3 and Pt (Figure 7c), which hinders the flow of photogenerated electrons from WO_3 to Pt. We conclude therefore that, whereas inserting a Pt layer promotes the separation of photogenerated charge carriers in n-Si, it hinders the same in WO_3. Nevertheless, the first effect is dominant over the latter, so overall the insertion of a Pt layer is beneficial.

Figure 7e shows the PEC performance measured under chopped simulated sunlight. The photocurrent density of WO_3/Pt/n-Si is 0.19 mA/cm^2 at 1.23 V vs RHE, which is almost two times larger than that in WO_3/n-Si. Moreover, upon further increasing the applied potential, the

photocurrent density of WO_3/Pt/n-Si increases steeply. It is 1.38 mA/cm^2 at 1.6 V vs RHE, which is about ten times higher than that in WO_3/n-Si. This rapid increase of the photocurrent in WO_3/Pt/n-Si is possibly related to the fact that the Schottky barrier at the interface of WO_3/Pt is overcome with a higher applied potential, which results in an easier transport of the photogenerated charge carriers.

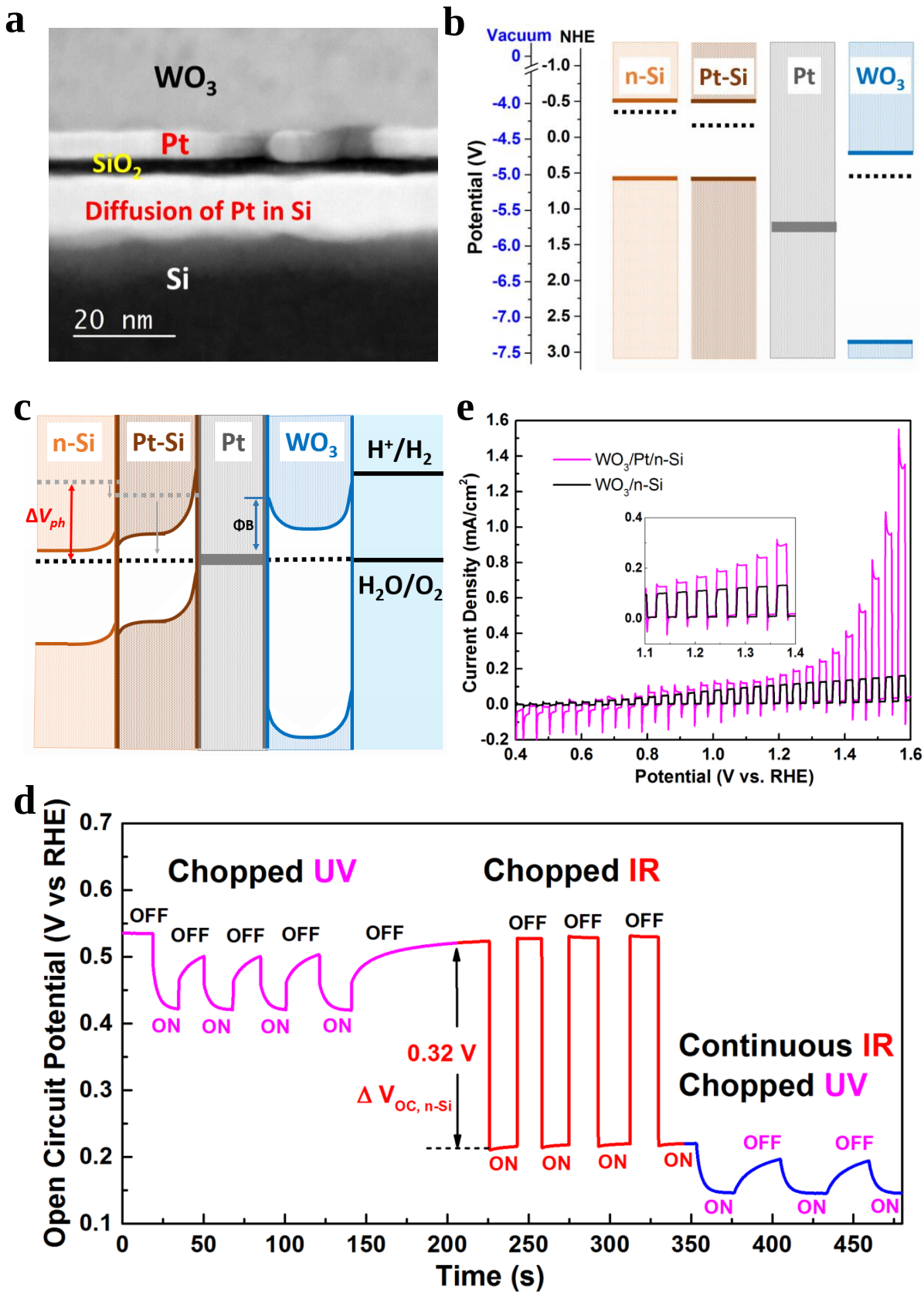

Figure 7. (a) Cross-section HAADF-STEM image of WO_3/Pt/n-Si. (b) Diagram of relative energy band levels of n-Si, Pt-Si (diffusion of Pt in n-Si), Pt and WO_3. (c) Schematic band diagram of WO_3/Pt/n-Si in equilibrium in the dark. (d) Open circuit potential (V_{OC}) versus elapsed time for WO_3/Pt/n-Si under chopped UV illumination (purple), chopped IR

illumination (red), and chopped UV with a continuous IR illumination (blue). (e) Photocurrent density vs. applied potential curves under chopped simulated sun light illumination (cycles of 2s light on and 2s light off) for WO_3/Pt/n-Si (purple) compared with WO_3/n-Si (black) (Inset: enlargement of the curves at 1.1 – 1.4 V vs. RHE).

3. Conclusion

In summary, we apply separate monochromatic UV and IR illumination on a WO_3/n-Si heterostructure and prove experimentally that the photogenerated charge carriers generated in the n-Si substrate contribute indirectly to the PEC water oxidation. By measuring the photovoltage under chopped monochromatic illumination, we find that the Si provides a photovoltage which drives the charge carriers for the PEC water splitting process.

Equilibration of the Fermi levels in WO_3 and n-Si induces band bendings in the semiconductors. These generate an internal electric field that is instrumental in separating the photogenerated charge carriers and setting up the photovoltage. To further study the relation between the heterojunction band structure and the PEC activity, we fabricate WO_3/Ag/n-Si heterostructures with a metal Ag interface layer between the semiconductors. Within the Z scheme, such an interface layer is predicted to enhance the PEC activity, because it facilitates charge transport. However, we measure a PEC activity in WO_3/Ag/n-Si that is lower than that in WO_3/n-Si. We attribute this to a decrease of the photovoltage, which is caused by a reduction of the band bending in the n-Si due to the Ag layer. This discovery breaks through the existing design ideas, which focused on facilitating charge transport via interface layers within the Z-scheme, but ignored the resulting changes in the potential profiles, the band bending in particular.

We evaluate what the effect is of the native SiO_2 layer, which covers the n-Si. To this end, we remove the SiO_2 by in-situ ion beam milling (IBM), before sputtering the Ag layer. We find actually that these WO_3/Ag/(IBM)n-Si devices have a worse PEC activity than the original WO_3/Ag/n-Si devices, which have a thin SiO_2 layer between Ag and n-Si. We attribute this to

the existence of midgap states at the Ag/n-Si interface, which lead to an increase the recombination of photogenerated electrons and holes. The SiO_2 layer passivates these states and should therefore be retained for metal/Si based photoelectrodes.

Based on all these findings, we fabricate WO_3/Pt/n-Si photoelectrodes, using native oxidized n-Si as substrate. The high work-function metal Pt is supposed to enlarge the band bending in n-Si, which increases the internal electric field, and therefore the charge carrier separation and the photovoltage. Compared to WO_3/n-Si, these WO_3/Pt/n-Si photoelectrodes achieve indeed a two times enhancement of photocurrent density at 1.23 V vs RHE and a ten times enhancement at 1.6 V vs RHE. One slight drawback of the Pt layer is the emergence of a Schottky barrier with the WO_3 that partially hinders the charge transport.

The latter points out a promising direction in the design of metal oxide/n-Si photoanodes for PEC applications. The band bending in Si can be enlarged by inserting thin metal films with relatively high work function between the Si and the metal oxide. To make further progress the metal/metal oxide interfaces should be modified to an ohmic contact to enhance the charge transport.

4. Experimental Section

Fabrication of WO_3/FTO, WO_3/n-Si, and WO_3/X/n-Si (X = Ag, Pt): the FTO used in this work is about 400 nm thick and coated on 1 mm thick glass (FTO15, Pilkington). The procedure described by Malviya et al[50] was followed for the cleaning of the FTO substrates. The n-Si substrates (n-doped, <100> orientation, resistivity 1-10 Ω cm, 280 μm-thick, single side polished, University Wafer) were cleaned sequentially in an ultrasonic bath of isopropanol and distilled (DI) water for 20 min.

WO_3 films were deposited by reactive RF sputtering in a 40/10 sccm Ar/O_2 mixture, where the O_2 was inserted at the sample position and the Ar at the W target. A Bestec GmBH

sputter tool was used with a 2 inch metallic tungsten target at a target−substrate distance of ~100 mm. The main deposition parameters are listed in Table S1.

For WO_3/Ag/n-Si and WO_3/Pt/WO_3 devices, the Ag and Pt films were both deposited by DC sputtering (50 sccm Ar) using the same tool. The metal depositions were carried out directly before the WO_3 deposition without breaking the vacuum.

To study the role of the native SiO_2 layer, WO_3/Ag/n-Si photoelectrodes without native SiO_2 layer were fabricated. In order to remove the native oxide layer on n-Si, the n-Si was treated by ion beam milling (IBM) by a Kaufman source at 1 kV for 2 min in the same vacuum system as the sputtering chamber. Figure S1 shows the flow diagram of deposition.

All WO_3/substrate samples were annealed at 450°C in Ar for 1 h with a ramping rate of 5°C/min using a tubular furnace with a quartz tube (Carbolite Gero). The Ar gas flow was started 30 min prior to annealing to guarantee a stable gas atmosphere.

Characterization: The surface and cross-sectional morphologies of the WO_3/n-Si and WO_3/FTO devices were investigated by a field emission scanning electron microscope (SEM) (Zeiss Sigma, Germany) with an in-lens detector and 5 kV accelerating voltage. A 10 nm Cr layer is coated on the top of the WO_3/n-Si and WO_3/FTO to enhance the conductivity before SEM analysis. A probe corrected JEOL ARM200F transmission electron microscope (TEM) is used to evaluate the cross-sectional morphologies of the WO_3/n-Si, WO_3/FTO and WO_3/Pt/n-Si devices. Cross-sectional TEM sample preparation was performed using a focused ion beam (FIB) (FEI, the Netherlands) using a standard lift-out procedure. The valence state of Si before IBM treatment was analyzed using a Thermo Scientific Kα X-ray photoelectron spectroscopy (XPS) setup with an Al Kα source ($h\nu$ = 1486.6 eV). After IBM treatment, the valence state of the Si was checked again using an in-situ XPS setup (Al Kα source, $h\nu$ = 1486.6 eV), which is connected to the IBM chamber and sputtering chamber and in the same vacuum system. The

binding energy was calibrated according to the signal of adventitious carbon (binding energy = 284.8 eV).

Photoelectrochemical measurements: A three-electrode PEC cell with a quartz window was used to measure the PEC performance at room temperature. Sunlight illumination was simulated using an AM 1.5 class A solar simulator (LCS 100, Oriel Instruments), which uses a 100 W Xe lamp with a calibrated illumination intensity of 100 mW cm^{-2} at the sample position. The light source was calibrated with a calibrated reference cell and meter (Newport, model 91150 V). Chopped simulated sunlight illumination was performed with an externally controlled shutter at a rate of 0.5 s^{-1}. Monochromatic light illumination was realized using a separately controlled UV lamp (λ = 365 nm, 9 mW) and an IR laser (λ = 960 nm, cw, 200 mW) as light sources. A long-pass dichroic mirror (cut-off wavelength 600 nm, Thorlabs) was used to combine the UV and the IR beams to one beam. The WO_3/substrate working electrodes were encapsulated in epoxy (Loctite EA 9492), resulting in an exposed active area of about 0.25 cm^2. The exact geometrical area of the exposed electrode surface was determined by calibrated digital images and ImageJ. A coiled Pt wire (0.8 mm in thickness) and an Ag/AgCl/Sat. KCl electrode (XR 300, Radiometer Analytical) were used as the counter electrode and the reference electrode, respectively. An aqueous solution of 0.5 M H_2SO_4 (pH ~0.3) was used as electrolyte. The potential of the electrode was controlled with a BioLogic SP-150 potentiostat. All potentials reported in the PEC results in this study are given with respect to the reversible hydrogen electrode (RHE) through the relation[37]

$$\Phi_{RHE} = \Phi_{Ag/AgCl} + \Phi^{o}_{Ag/AgCl\ vs\ RHE} + 0.059 \times pH, \qquad (1)$$

where $\Phi^{o}_{Ag/AgCl}$ is 0.197 V versus RHE at 25°C. Linear sweep voltammetry (LSV) measurements were performed at potentials between 0.4 V and 1.6 V versus RHE at a scan rate of 10 mV s^{-1}.

Supporting Information
Supporting Information is available from the Wiley Online Library or from the author.

Acknowledgements

Y. Zhao and A. Bieberle-Hütter acknowledge the financial support from NWO (FOM program nr. 147 "CO_2 neutral fuels") and from the China Scholarship Council (CSC). The authors thank Nanolab at TU/e for access to SEM. We thank Erwin Zoethout (DIFFER) for performing the XPS of original Si and for preparing the WO_3/Pt/n-Si lamella for TEM, Beatriz Barcones (TU/e) for preparing the WO_3/n-Si and WO_3/FTO lamellas for TEM, Stefan C. J. Meskers (TU/e) for the IR laser, and Michail Tsampas (DIFFER) for the UV lamp. Solliance and the Dutch province of Noord-Brabant are acknowledged for funding the TEM facility.

Received: ((will be filled in by the editorial staff))
Revised: ((will be filled in by the editorial staff))
Published online: ((will be filled in by the editorial staff))

References

[1] A. Fujishima, K. Honda, *Nature* **1972**, *238*, 37.

[2] Nathan S. Lewis, *Science* **2016**, *351*, aad1920.

[3] R. van de Krol, Y. Liang, J. Schoonman, *J. Mater. Chem.* **2008**, *18*, 2311.

[4] O. Khaselev, J. A. Turner, *Science* **1998**, *280*, 425.

[5] K. Sivula, R. van de Krol, *Nat. Rev. Mater.* **2016**, *1*, 15010.

[6] Y. J. Hwang, A. Boukai, P. Yang, *Nano Lett.* **2009**, *9*, 410.

[7] S. Kuang, L. Yang, S. Luo, Q. Cai, *Appl. Surf. Sci.* **2009**, *255*, 7385.

[8] Y. Lin, Y. Xu, M. T. Mayer, Z. I. Simpson, G. McMahon, S. Zhou, D. Wang, *J. Am. Chem. Soc.* **2012**, *134*, 5508.

[9] Y. Zhao, K. R. Yang, Z. Wang, X. Yan, S. Cao, Y. Ye, Q. Dong, X. Zhang, J. E. Thorne, L. Jin, K. L. Materna, A. Trimpalis, H. Bai, S. C. Fakra, X. Zhong, P. Wang, X. Pan, J. Guo, M. Flytzani-Stephanopoulos, G. W. Brudvig, V. S. Batista, D. Wang, *Proc. Natl. Acad. Sci.* **2018**, 201722137.

[10] J. Y. Zheng, G. Song, C. W. Kim, Y. S. Kang, *Nanoscale* **2013**, *5*, 5279.

[11] K. Yuan, Q. Cao, X. Li, H. Y. Chen, Y. Deng, Y. Y. Wang, W. Luo, H. L. Lu, D. W. Zhang, *Nano Energy* **2017**, *41*, 543.

[12] C. A. Bignozzi, S. Caramori, V. Cristino, R. Argazzi, L. Meda, A. Tacca, *Chem. Soc. Rev.* **2013**, *42*, 2228.

[13] D. Barreca, G. Carraro, A. Gasparotto, C. Maccato, T. Altantzis, C. Sada, K. Kaunisto, T. P. Ruoko, S. Bals, *Adv. Mater. Interfaces* **2017**, *4*, 1.

[14] M. Li, L. Zhao, L. Guo, *Int. J. Hydrogen Energy* **2010**, *35*, 7127.

[15] S. Y. Noh, K. Sun, C. Choi, M. Niu, M. Yang, K. Xu, S. Jin, D. Wang, *Nano Energy* **2013**, *2*, 351.

[16] Y. Yu, Z. Zhang, X. Yin, A. Kvit, Q. Liao, Z. Kang, X. Yan, Y. Zhang, X. Wang, *Nat. Energy* **2017**, *2*, 17045.

[17] P. Leempoel, M. Castro-Acuna, F. R. F. Fan, A. J. Bard, *J. Phys. Chem.* **1982**, *86*, 1396.

[18] Y. W. Chen, J. D. Prange, S. Dühnen, Y. Park, M. Gunji, C. E. D. Chidsey, P. C. McIntyre, *Nat. Mater.* **2011**, *10*, 539.

[19] R. van de Krol, Y. Liang, *Chim. Int. J. Chem.* **2013**, *67*, 168.

[20] R. H. Coridan, M. Shaner, C. Wiggenhorn, B. S. Brunschwig, N. S. Lewis, *J. Phys. Chem. C* **2013**, *117*, 6949−6957.

[21] C. J. Z. Xing, S. Shen, M. Wang, F. Ren, Y. Liu, X. Zheng, Y. Liu, X. Xiao, W. Wu, *Appl. Phys. Lett.* **2015**, *105*, 143902.

[22] S. K. Chong, C. F. Dee, S. A. Rahman, *RSC Adv.* **2015**, *5*, 2346.

[23] M. T. Mayer, C. Du, D. Wang, *J. Am. Chem. Soc.* **2012**, *134*, 12406.

[24] Q. Mi, Y. Ping, Y. Li, B. Cao, B. S. Brunschwig, P. G. Khalifah, G. a Galli, H. B. Gray, N. S. Lewis, *J. Am. Chem. Soc.* **2012**, *134*, 18318.

[25] J. Y. Zheng, Z. Haider, T. K. Van, A. U. Pawar, M. J. Kang, C. W. Kim, Y. S. Kang, *CrystEngComm* **2015**, *17*, 6070.

[26] M. R. Shaner, K. T. Fountaine, S. Ardo, R. H. Coridan, H. a. Atwater, N. S. Lewis, *Energy Environ. Sci.* **2014**, *7*, 779.

[27] A. Kargar, S. J. Kim, P. Allameh, C. Choi, N. Park, H. Jeong, Y. Pak, G. Y. Jung, X. Pan, D. Wang, S. Jin, *Adv. Funct. Mater.* **2015**, *25*, 2609.

[28] R. H. Coridan, K. a Arpin, B. S. Brunschwig, P. V Braun, N. S. Lewis, *Nano Lett.* **2014**, *14*, 2310.

[29] S. Y. Reece, J. a. Hamel, K. Sung, T. D. Jarvi, a. J. Esswein, J. J. H. Pijpers, D. G. Nocera, *Science* **2011**, *334*, 645.

[30] Y. Yu, Z. Zhang, X. Yin, A. Kvit, Q. Liao, Z. Kang, X. Yan, Y. Zhang, X. Wang, *Nat. Energy* **2017**, *2*, 17045.

[31] M. Yoshimizu, Y. Hotori, H. Irie, *J. Mater. Sci. Chem. Eng.* **2017**, *05*, 33.

[32] T. Zhu, M. N. Chong, E. S. Chan, *ChemSusChem* **2014**, *7*, 2974.

[33] G. Carraro, A. Gasparotto, C. Maccato, E. Bontempi, D. Barreca, *Chem. Vap. Depos.* **2015**, *21*, 294.

[34] D. Valerini, S. Hernandez, F. Di Benedetto, N. Russo, G. Saracco, A. Rizzo, *Mater. Sci. Semicond. Process.* **2016**, *42*, 150.

[35] T. Stoll, G. Zafeiropoulos, I. Dogan, H. Genuit, R. Lavrijsen, B. Koopmans, M. N. Tsampas, *Electrochem. commun.* **2017**, *82*, 47.

[36] Y. Zhao, S. Balasubramanyam, R. Sinha, R. Lavrijsen, M. A. Verheijen, A. A. Bol, A. Bieberle-hu, *ACS Appl. Energy Mater.* **2018**, *1*, 5887.

[37] H. L. Tuller, *Photoelectrochemical Hydrogen Production*; Krol, R. van de; Grätzel, M., Eds.; Electronic Materials: Science & Technology; Springer US: Boston, MA, 2012; Vol. 102.

[38] Y. Bu, Z. Chen, C. Sun, *Appl. Catal. B Environ.* **2015**, *179*, 363.

[39] M. R. Elahifard, S. Rahimnejad, S. Haghighi, M. R. Gholami, *J. Am. Chem. Soc.* **2007**, *129*, 9552.

[40] L. Ye, J. Liu, C. Gong, L. Tian, T. Peng, L. Zan, *ACS Catal.* **2012**, *2*, 1677.

[41] J. Hölzl, F. K. Schulte, H. Wagner, *Solid Surface Physics*; Springer-Verlag Berlin, 1979.

[42] C. Ballif, D. M. Huljić, G. Willeke, A. Hessler-Wyser, *Appl. Phys. Lett.* **2003**, *82*, 1878.

[43] A. Thanailakis, A. Rasul, J. D. Mottram, D. C. Northrop, E. H. Rhoderick, *J. Phys. C Solid State Phys.* **1975**, *8*, 655.

[44] N. Koshizaki, H. Umehara, T. Oyama, *Thin Solid Films* **1998**, *325*, 130.

[45] D. S. Jensen, S. S. Kanyal, N. Madaan, M. A. Vail, A. E. Dadson, M. H. Engelhard, M. R. Linford, *Surf. Sci. Spectra* **2013**, *20*, 36.

[46] R. Elbersen, W. Vijselaar, R. M. Tiggelaar, H. Gardeniers, J. Huskens, *Adv. Mater.* **2015**, *27*, 6781.

[47] W. Liu, F. Meng, X. Zhang, Z. Liu, *ACS Appl. Mater. Interfaces* **2015**, *7*, 26522.

[48] E. Conforto, P. E. Schmid, *Philos. Mag. A Phys. Condens. Matter, Struct. Defects Mech. Prop.* **2001**, *81*, 61.

[49] S. Mantovani, F. Nava, C. Nobili, G. Ottaviani, *Phys. Rev. B* **1986**, *33*, 5536.

[50] K. D. Malviya, H. Dotan, K. R. Yoon, I.-D. Kim, A. Rothschild, *J. Mater. Res.* **2016**, *31*, 1565.

Supporting Information

Boosting the Performance of WO_3/n-Si for Photo-electrochemical Water Splitting: the Role of Si to Interface Engineering

*Yihui Zhao, Geert Brocks, Han Genuit, Reinoud Lavrijsen, Marcel A Verheijen, Anja Bieberle-Hütter**

Films deposition

Table 1

Sputtering process parameters for WO_3 deposition.

Parameter	Value
Target power	100 W
Base pressure	$<10^{-8}$ mbar
Deposition pressure	10^{-2} mbar
Substrate temperature	Room temperature
O_2 flow rate	10 sccm
Ar flow rate	40 sccm

Figure S1 shows the flow diagram of the thin film depositions.

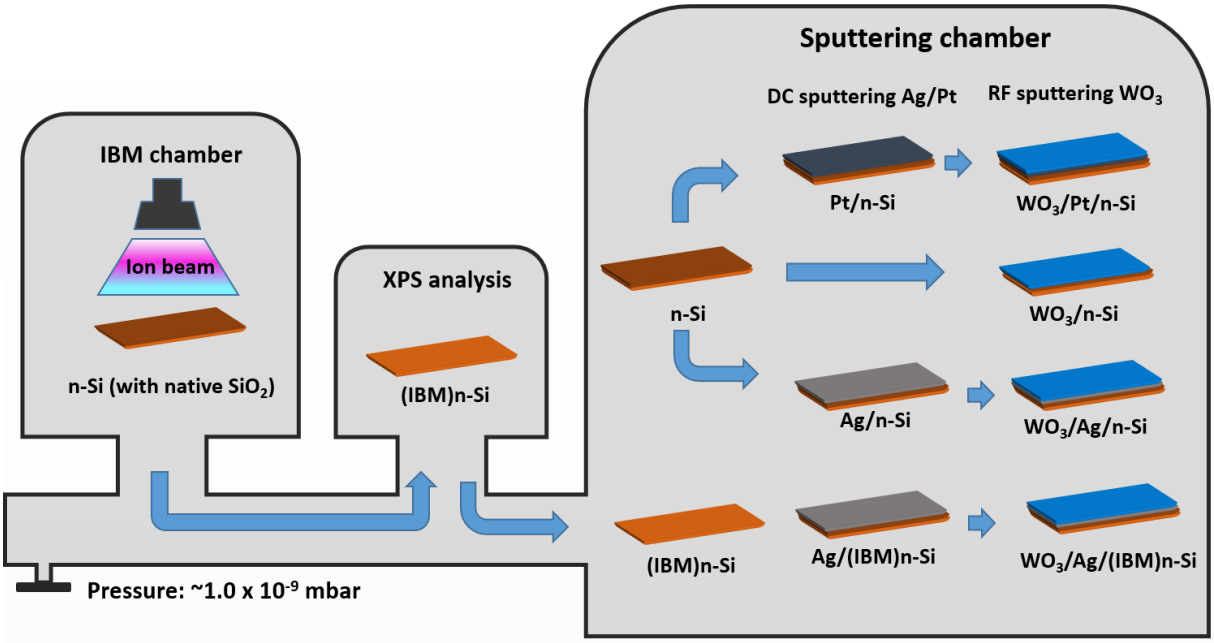

Figure S1: Flow diagram of WO_3/n-Si, WO_3/Ag/n-Si, WO_3/Ag/(IBM)n-Si (ion beam milling treated n-Si) and WO_3/Pt/n-Si deposition. The entire process is carried out without breaking the vacuum.

Atomic Force Microscope (AFM) of WO_3/n-Si and WO_3/FTO

Figure S2 shows the surface roughnesses of WO_3/n-Si and WO_3/FTO, which were measured by AFM. The surface roughnesses of WO_3/n-Si and WO_3/FTO are R_a = 2.2 nm and R_a = 7.1 nm, respectively.

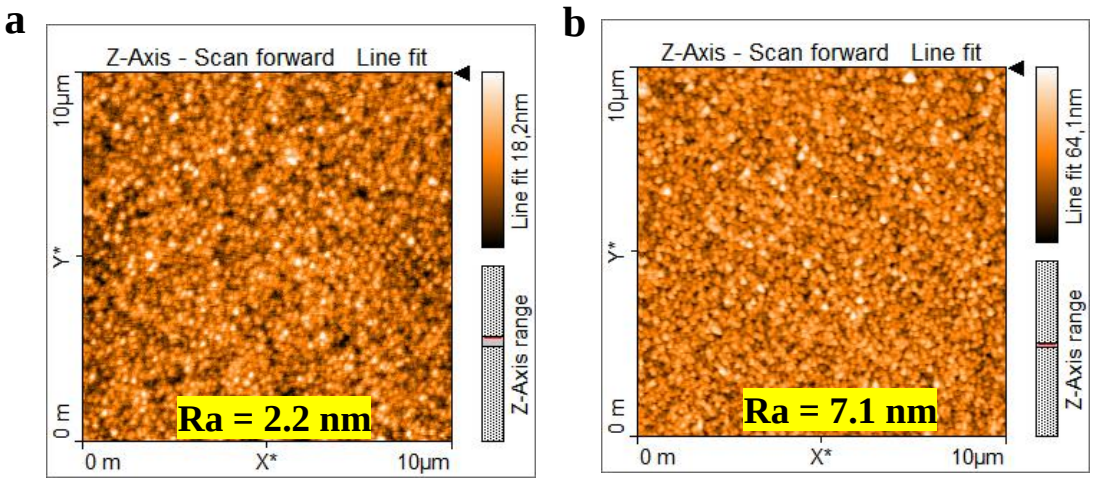

Figure S2: Atomic Force Microscope (AFM) of (a) WO_3/n-Si and (b) WO_3/FTO after annealing in the Ar.

Cross-section HAADF-STEM of WO_3/n-Si and WO_3/FTO

Cross-section HAADF-STEM images confirm that an intimate contact is obtained for both WO_3/n-Si and WO_3/FTO interfaces, as shown in Figure S3.

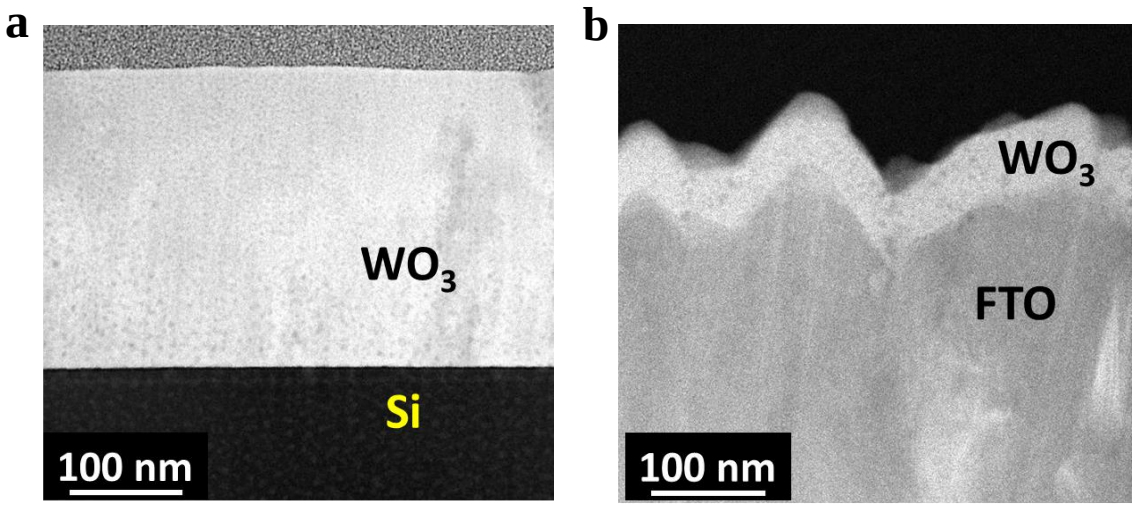

Figure S3: Cross-section HAADF-STEM images of (a) WO_3/n-Si and (b) WO_3/FTO.

GIXRD of WO_3/n-Si and WO_3/FTO

The GIXRD spectra of the WO_3/n-Si and WO_3/FTO after annealing in Ar at 450℃ for 1 h are shown in Figure S4. The diffraction peaks agree well with monoclinic WO_3 corresponding to JCPDS No. 83-0950 indicating that monoclinic WO_3 was obtained for both electrodes after annealing.

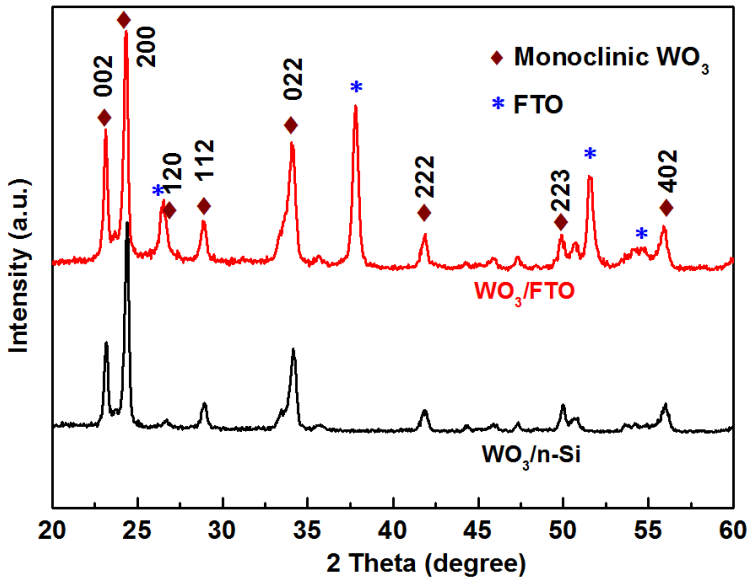

Figure S4: GIXRD spectra of WO_3/n-Si (black) and WO_3/FTO (red) after annealing in Ar. The brown diamonds and the blue dots are monoclinic WO_3 (JCPDS No. 83-0950) and FTO (JCPDS No. 83-0950), respectively.

Relative energy band levels

Figure S5 shows the energy band diagrams of n-Si, WO_3, Ag, Pt and H_2O. The band gap of n-Si is ~1.1 eV[1] and the Fermi level is about -4.25 ± 0.1 eV vs vacuum level[1–3]. The band gap of WO_3 is about 2.8 - 3.0 eV and the Fermi level is about -5.25 ± 0.1 eV[4–7]. The work functions of Ag and Pt are 4.5 ± 0.15 eV and 5.7 ± 0.1 eV vs vacuum level[8].

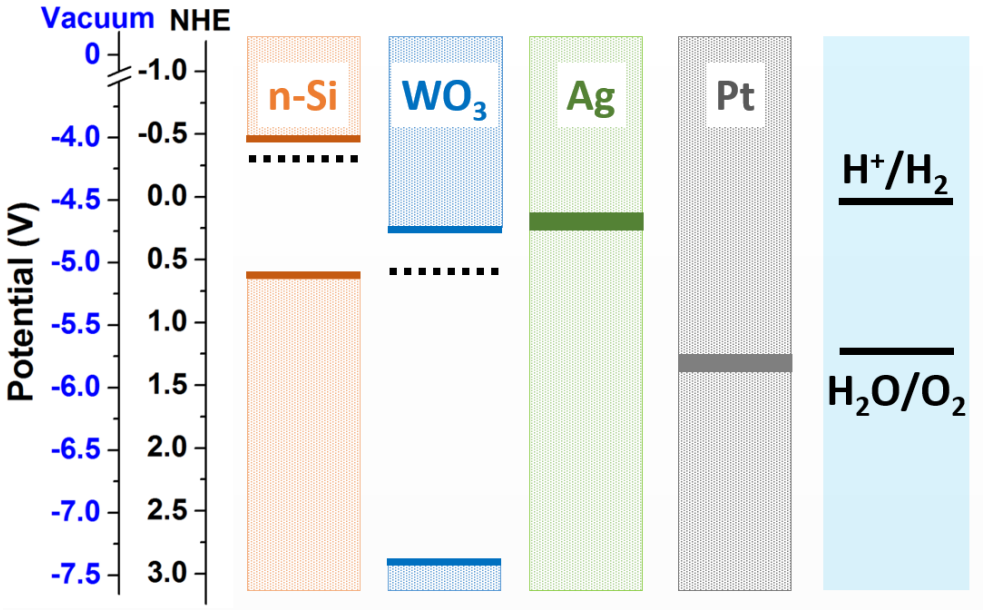

Figure S5: Diagram of relative energy band levels of n-Si, WO_3, Ag, Pt, and H_2O. The diagram is constructed from literature data[1–8].

Reference

[1] S. Y. Reece, J. a. Hamel, K. Sung, T. D. Jarvi, a. J. Esswein, J. J. H. Pijpers, D. G. Nocera, *Science* **2011**, *334*, 645.

[2] M. T. Mayer, C. Du, D. Wang, *J. Am. Chem. Soc.* **2012**, *134*, 12406.

[3] Y. J. Hwang, A. Boukai, P. Yang, *Nano Lett.* **2009**, *9*, 410.

[4] Y. Zhao, S. Balasubramanyam, R. Sinha, R. Lavrijsen, M. A. Verheijen, A. A. Bol, A. Bieberle-Hütter, *ACS Appl. Energy Mater.* **2018**, *1*, 5887.

[5] P. Dias, T. Lopes, L. Meda, L. Andrade, A. Mendes, *Phys. Chem. Chem. Phys.* **2016**, 5232.

[6] H. Li, H. Yu, X. Quan, S. Chen, Y. Zhang, *ACS Appl. Mater. Interfaces* **2016**, *8*, 2111.

[7] J. Y. Zheng, A. U. Pawar, C. W. Kim, Y. J. Kim, Y. S. Kang, *Appl. Catal. B Environ.* **2018**, *233*, 88.

[8] J. Hölzl, F. K. Schulte, H. Wagner, *Solid Surface Physics*; Springer-Verlag Berlin, 1979.